



HAL
open science

Effects of Pd and Co intimacy in Pd-modified Co/TiO₂ catalysts for direct CO₂ hydrogenation to fuels: the closer not the better

Canio Scarfiello, Aurélien Durupt, Yann Tison, Doan Pham Minh, Katerina Soulantica, Philippe Serp

► To cite this version:

Canio Scarfiello, Aurélien Durupt, Yann Tison, Doan Pham Minh, Katerina Soulantica, et al.. Effects of Pd and Co intimacy in Pd-modified Co/TiO₂ catalysts for direct CO₂ hydrogenation to fuels: the closer not the better. *Catalysis Science & Technology*, 2024, 14 (10), pp.2896-2907. 10.1039/D4CY00324A . hal-04552701

HAL Id: hal-04552701


<https://hal.science/hal-04552701v1>

Submitted on 30 Apr 2024

HAL is a multi-disciplinary open access archive for the deposit and dissemination of scientific research documents, whether they are published or not. The documents may come from teaching and research institutions in France or abroad, or from public or private research centers.

L'archive ouverte pluridisciplinaire **HAL**, est destinée au dépôt et à la diffusion de documents scientifiques de niveau recherche, publiés ou non, émanant des établissements d'enseignement et de recherche français ou étrangers, des laboratoires publics ou privés.

Effects of Pd and Co intimacy in Pd-modified Co/TiO₂ catalysts for direct CO₂ hydrogenation to fuels: the closer not the better†

Canio Scarfiello,^{abc} Aurélien Durupt,^{abc} Yann Tison,^d Doan Pham Minh,^a Katerina Soulantica^b and Philippe Serp^c 

Direct CO₂ hydrogenation to liquid fuels is a sustainable approach to decarbonize the future air transport. This reaction proceeds through a tandem pathway involving the reverse water gas shift reaction (RWGSR) to produce CO and the subsequent traditional CO-Fischer-Tropsch synthesis. On Co-based catalysts, the introduction of dopants can improve CO₂ activation, enhance the RWGSR activity and decrease the methanation side reaction. We reported that alkali-promoted Co/TiO₂ catalysts outperform the unpromoted ones in terms of activity and selectivity towards C₂₊ (C. Scarfiello, K. Soulantica, S. Cayez, A. Durupt, G. Viau, N. Le Breton, A. K. Boudalis, F. Meunier, G. Clet, M. Barreau, D. Salusso, S. Zafeiratos, D. P. Minh and P. Serp, *J. Catal.*, 2023, **428**, 115202). To further improve the catalytic performances, we doped an alkali-promoted Co/TiO₂ catalyst with palladium, which is active for the RWGSR and promotes hydrogen spillover. The effect of noble metal location in relation to cobalt, a rarely studied parameter, was investigated by using bimetallic and mixtures of monometallic catalysts. This study demonstrates that whatever the location of Pd and its loading (0.03–0.9 wt%), doping with this metal leads to an improvement in catalytic activity. Furthermore, we show that the proximity between Co and Pd has a pronounced effect on the selectivity of the reaction. The best configuration to achieve higher activity and C₂₊ selectivity is obtained using mixtures of monometallic catalysts.

1. Introduction

The direct CO₂ conversion to liquid fuels by catalytic hydrogenation (CO₂-based Fischer-Tropsch synthesis, CO₂-FTS), is a sustainable approach to reduce CO₂ emissions toward net-zero emissions by 2050.¹ This challenging reaction proceeds through tandem catalysis involving the endothermic reverse water gas shift reaction (RWGSR) to produce CO and the subsequent traditional exothermic CO-FTS. The synthetic fuels resulting from this process can contribute to accelerating the decarbonization of aviation fuels.² Carbon dioxide can be hydrogenated into hydrocarbons on Co-³ or Fe-based⁴ catalysts by direct or indirect routes. The direct route (CO₂-FTS route) is a combination in a single reactor of

the reduction of CO₂ to CO and the subsequent hydrogenation of CO into hydrocarbons at a given temperature and pressure. The indirect route is carried out using two different reactors to perform the RWGSR and CO-FTS under different conditions. Compared to the latter, the direct route should be more economical and energy efficient for the production of kerosene-type hydrocarbons.⁵ An inherent constraint of the CO₂-FTS route is that the RWGS equilibrium is favorable at much higher temperatures than hydrocarbon chain growth for classical FTS-type catalysts.⁶ This is particularly true for Co-based catalysts, which show superior ability for chain growth, stability, and lower activity for the WGS reaction and require milder operating conditions than Fe-based catalysts.^{7,8} In addition, the thermal stability of CO₂, the weak CO₂ adsorption, the operating conditions and RWGS thermodynamic constraints lead to low CO coverage on Co-based catalysts, resulting in the preferential production of CH₄ and short chain hydrocarbons.^{3,9} Consequently, avoiding the undesired methanation of CO₂ and developing low-temperature RWGSR catalysts constitute significant challenges of the CO₂-FTS route on Co-based catalysts.⁸

It is known that alkalized cobalt catalysts can be active for the catalytic hydrogenation of CO₂ to higher hydrocarbons.¹⁰ We recently showed that a careful choice of the metal oxide

^a Université de Toulouse, IMT Mines Albi, UMR CNRS 5302, Centre RAPSODEE, Campus Jarlard, F-81013 Albi, Cedex 09, France

^b Université de Toulouse, INSA, UPS, CNRS, LPCNO, 135 avenue de Rangueil, F-31077 Toulouse, France

^c LCC, CNRS-UPR 8241, ENSIACET, Université de Toulouse, France.

E-mail: philippe.serp@ensiacet.fr

^d IPREM CNRS UMR 5254, Université de Pau et des Pays de l'Adour, Pau 64053, France

† Electronic supplementary information (ESI) available. See DOI: <https://doi.org/10.1039/d4cy00324a>

support and the alkali metal promoter and the regulation of the metal–support interface allow increasing the selectivity towards higher hydrocarbons.¹¹ Thus, on Na-promoted Co/TiO₂ catalysts, the C₂₊ selectivity can reach 45%, whereas it is only 5% on the unpromoted catalysts. A potential approach to further improvement of the catalytic performance, could be to dope cobalt with a cocatalyst. This dopant should be able to (i) catalyze efficiently the RWGSR and (ii) favor the hydrogen spillover (H-spillover), which can contribute to maintaining a high degree of cobalt reduction necessary for paraffin production by FTS.¹² The choice of a noble metal should be appropriate since noble metals (i) are proven to be highly active RWGSR catalysts,¹³ (ii) are used to promote Co-based catalysts on non-reducible oxides for low-pressure CO₂ hydrogenation,^{14,15} and (iii) are regularly employed to promote Co-based CO-FTS catalysts by improving the cobalt reducibility thanks to H-spillover.^{16,17} Spillover H species resulting from the presence of Pd in alkali-promoted iron catalysts were reported to be involved in CO₂-FTS, contributing to performance enhancement.¹⁸

CO₂ reduction to CO/CH₄ is a complex process and generally proceeds *via* the initial reduction to *CO (adsorbed CO species), which can then desorb or be hydrogenated to CH₄.¹⁹ The adsorption strength of *CO is therefore a crucial factor. Transition metals with relatively high CO adsorption energy, namely Pt, Pd, Ni, Rh, Fe, Co and Ru, tend to catalyze both RWGSR and methanation.²⁰ However, structure sensitivity has been reported for CO₂ hydrogenation.^{21,22} Strong interaction of CO with large metal particles facilitates C≡O bond dissociation, which favors CH₄ formation. Conversely, weak interaction leads either to the desorption of CO or the formation of alcohols and aldehydes.²⁰ Palladium is not normally employed as a RWGSR catalyst because of its high selectivity towards CH₄.²³ However, highly dispersed Pd/Al₂O₃ catalysts²⁴ or Pd single atoms dispersed on TiO₂²⁵ are more selective towards CO. Similarly, while relatively large Pt particles produce mainly CH₄,²⁶ Pt single atoms on TiO₂ are active sites for CO formation.²⁷ A similar behavior has been reported for rhodium catalysts on TiO₂.^{28–30} On Ni, the decreased methanation activity and the related higher CO selectivity on small particles was linked to a lower availability of step edges, which are active for CO dissociation.²¹ Finally, the CO adsorption strength can be weakened *via* strong metal–support interactions (SMSI) and/or the formation of metal alloys.^{19,31,32}

In this context, in the present study we report the catalytic performances of Na-promoted and Pd-doped Co/TiO₂ catalysts for CO₂-FTS. Two systems were investigated: bimetallic catalysts and mixtures of monometallic catalysts. For bimetallic Pd–Co catalysts, the effects of both Pd location with respect to Co, and Pd loading, were investigated. The separation of the two metals on two different supports has been tested with two different configurations of the catalytic bed: (i) the two catalysts are placed in two distinct layers (2 beds); and (ii) the two powders are physically mixed. These different systems allow the intimacy between Pd and Co to be varied from “closest” to “nanoscale” and “milliscale”

distance. Few studies have focused on the intimacy criterion between cobalt and a noble metal for the CO-FTS, which pointed to a better Co reducibility when Co and noble metal particles were in direct contact.^{33,34} Herein we show that the separation of the two metals over “milliscale” distances can benefit STY and S_{C₂₊}.

2. Materials and methods

2.1 Support and catalyst preparation

TiO₂* support. 1 g of NaBH₄ was dissolved in 50 mL of EtOH in a rotavapor flask. Then, 10 g of TiO₂-P25 were added to the solution. The mixture was stirred in the rotavapor for 1 h (25 °C, 500 mbar). Subsequently, the EtOH was removed using the rotavapor (80 °C, 150 mbar for 30 min and then 75 mbar for 30 min). The resulting powder was dried overnight at 120 °C in a static oven, ground and then treated in a tubular oven under argon at 320 °C for 15 min (5 °C min⁻¹ ramp). The resulting blue product was recovered under argon and then washed four times with distilled water, followed by washing with absolute ethanol. Finally, the product was dried for 15 h at 150 °C under argon (5 °C min⁻¹ ramp).

Cobalt catalyst. The 10Co/TiO₂* catalyst with a loading of ~10 wt% was prepared by incipient wetness impregnation. 10 g of the TiO₂* support was placed in a Schlenk vessel and degassed for 2 h under vacuum at 150 °C (oil bath temperature). After cooling at room temperature, an aqueous metal precursor solution (Co(NO₃)₂·6H₂O) was added under vacuum with continuous stirring. The resulting mixture was sonicated for 30 min, followed by 30 min of stirring. The sonication/stirring sequence was repeated 4 times. The mixture was dried for 24 h at 80 °C followed by 12 h at 120 °C in a static furnace. Finally, the powder was treated in a tubular oven at 460 °C for 4 h under Ar (5 °C min⁻¹ ramp).

Palladium catalyst. The 1Pd/TiO₂* catalyst with a loading of ~1 wt% was prepared by wet impregnation. 10 g of the TiO₂* support was placed in a Schlenk flask and degassed for 2 h under vacuum at 150 °C (oil bath temperature). After cooling at room temperature, an aqueous metal precursor solution (Pd(NO₃)₂·xH₂O) was added under vacuum and with continuous stirring. The resulting mixture was stirred overnight. The powder was recovered *via* centrifugation and washed 6 times with distilled water. Finally, the powder was dried at 150 °C for 12 h under Ar and subsequently treated at 460 °C for 4 h under Ar.

Pd–Co catalysts. Pd deposition on the previously prepared 10Co/TiO₂* was performed by wet impregnation (0.1Pd–10Co-o/TiO₂* and 1Pd–10Co-o/TiO₂*) and galvanic displacement (0.1Pd–10Co-r/TiO₂*). For the 0.1Pd–10Co-o/TiO₂* and the 1Pd–10Co-o/TiO₂* catalysts, 10 g of the calcined monometallic Co-based catalyst (10Co₃O₄/TiO₂*) were placed in a Schlenk flask and degassed for 2 h under vacuum at 150 °C (oil bath temperature). After cooling at room temperature, an aqueous metal precursor solution (Pd(NO₃)₂·xH₂O) was added under vacuum and continuous stirring. The resulting mixture was stirred overnight. The powder was recovered *via*

centrifugation and washed 6 times with distilled water. Finally, the powder was dried at 150 °C for 12 h under Ar and subsequently treated at 460 °C for 4 h under Ar. For the 0.1Pd-10Co-r/TiO₂* catalyst, 10 g of 10Co₃O₄/TiO₂* catalyst were reduced at 350 °C for 4 h under flowing 40% H₂/Ar. After cooling, the powder was transferred to a Schlenk flask under Ar. An aqueous metal precursor solution (Pd(NO₃)₂·xH₂O) was added under vacuum and continuous stirring. The resulting mixture was stirred overnight. The powder was recovered *via* centrifugation and washed 6 times with distilled water. Finally, the powder was dried at 150 °C for 12 h under Ar and subsequently treated at 460 °C for 4 h under Ar.

Catalyst reduction. For the characterization of the reduced samples, 500 mg of catalyst were reduced in a tubular oven under a mixture of 40% H₂/Ar with a total flow of 25 mL min⁻¹.

2.2 Catalyst characterization

Transmission electron microscopy (TEM) and scanning transmission electron microscopy (STEM) studies were performed using a JEOL cold-FEG JEM-ARM200F microscope operated at 200 kV equipped with a probe Cs corrector reaching a spatial resolution of 0.078 nm. EDX spectra were recorded using a JEOL CENTURIO SDD detector. The TEM analysis was performed on catalyst samples after the reduction steps. The catalyst samples were prepared by ultrasound-assisted dispersion in pure ethanol, and the suspensions were dropped onto a holey carbon film-covered copper grid.

XRD measurements were performed using a PANalytical Empyrean diffractometer equipped with a Co radiation source ($l = 1.789 \text{ \AA}$). The diffraction patterns of supports and calcined and reduced catalysts were recorded within the 2θ range of 20–95° with an increment of 0.02° and 400 s per step. The Scherrer equation was used for the determination of crystallite size.

H₂-temperature-programmed reduction (TPR) measurements were performed using a Micromeritics AutoChem II 2920 analyzer. In a typical experiment, 50 mg of catalyst were placed on quartz wool into a U-tube quartz reactor. The sample was pretreated *in situ* by ramping at 10 °C min⁻¹ to 350 °C under a He flow and remained at that temperature for 60 min. Subsequently, the sample was cooled to 50 °C. At this temperature, a gas mixture of 5% H₂/N₂ passed through the sample with a total flow of 50 mL min⁻¹ and H₂-TPR was carried out by heating (10 °C min⁻¹) up to 900 °C. H₂ consumption was continuously monitored by a thermal conductivity detector.

CO₂-temperature-programmed desorption (TPD) measurements were carried out on a Micromeritics Autochem II 2920 instrument equipped with a thermal conductivity detector. In a typical experiment, 150 mg of reduced catalyst were placed on quartz wool into a U-tube quartz reactor. The sample was pretreated *in situ*

by ramping at 10 °C min⁻¹ to 350 °C in a He flow and remained at that temperature for 60 min. Subsequently, the sample was cooled to 50 °C. At this temperature, a gas mixture of 5% H₂/N₂ was sent on the sample with a total flow of 50 mL min⁻¹ and H₂-TPR was carried out by heating (10 °C min⁻¹) up to 350 °C and holding at this temperature for 30 min. H₂ consumption was continuously monitored by a thermal conductivity detector (TCD). Then, the gas flow was switched to He and held at 350 °C for 30 min. Subsequently, the sample was cooled to 50 °C. At this temperature, a gas mixture of 5% CO₂/N₂ was sent on the sample with a total flow of 50 mL min⁻¹ for 60 min. After saturation with CO₂, the sample was outgassed for 60 min at 50 °C under a He flow to ensure removal of physisorbed CO₂. Finally, the sample was heated under He up to 900 °C with a ramp of 10 °C min⁻¹ to measure CO₂ desorption (TCD).

X-ray photoelectron spectra were recorded on a Thermo Electron K α apparatus with a base pressure of 5×10^{-9} mbar. The incident photon energy was 1487 eV (Al K α). For high-resolution acquisition, the analyzer was set in CAE mode with a pass energy of 20 eV. Data processing was performed using CASAXPS. The analyses were performed with the introduction of the samples by a vacuum transfer cell from a glovebox under a controlled argon atmosphere so we can exclude air oxidation of these samples.

2.3 High-pressure catalytic tests

CO₂-FTS catalytic tests were performed in a high-pressure test rig.¹⁷ The reactor is composed of a stainless-steel tube of 33 cm length and 14 mm inner diameter. For a given CO₂-FTS catalytic test, the bottom part of the reactor was filled with sintered α -Al₂O₃ (1000 °C, 5 h) to sustain the catalytic bed. Then, 2 g of calcined catalyst were diluted with 8 g of inert SiC and placed in the middle of the stainless-steel reactor tube. The rest of the reactor tube was filled with calcined α -Al₂O₃. The separation between the filling material (α -Al₂O₃) and the catalyst was ensured by a layer of quartz wool. A thermocouple was placed at the center of the catalytic bed to control the reaction temperature. Each catalyst was reduced *in situ* at 350 °C for 4 h under 40% H₂/N₂ with a total flow of 100 mL min⁻¹. After reduction, the temperature was decreased to 220 °C and the catalyst was outgassed with N₂ to remove the excess H₂. Then, the gas was switched to a mixture of H₂/CO₂/N₂ = 36/18/18 mL min⁻¹ (H₂/CO₂ ratio 2:1). After 30 min, the pressure was slowly increased to 20 bar using a back-pressure controller. The test started once the desired pressure was reached.

The gaseous products were monitored every 30 min using an online μ -GC (Agilent 990) equipped with a MS5A SS (Ar carrier) column for the quantification of H₂, N₂, CH₄ and CO and a Poraplot U FS (He carrier) column for the quantification of CO₂, C₂H₄, C₂H₆, C₃H₈ and C₄H₁₀. Both columns are equipped with a TCD detector.

The calculation on the gaseous products detected by μ -GC was performed as follows.

N_2 was used as internal standard and the molar fraction of the different molecules during the CO_2 -FTS were calculated as follows:

$$Z^{out} (\text{mL min}^{-1}) = \frac{\% Z}{\% N_2^{out}} \cdot N_2^{in}$$

$Z^{out} = CO_2, H_2, CH_4, CO, C_2H_4, C_2H_6, C_3H_8, C_4H_{10}$.

$\% Z$ is obtained directly from the μ -GC, which has an internal calibration. $N_2^{in} = N_2$ input flow (mL min^{-1}).

CO_2 and H_2 conversions (X_{CO_2}, X_{H_2}) were calculated as follows:

$$X_{CO_2} (\%) = 100 \cdot \frac{CO_2^{in} - CO_2^{out}}{CO_2^{in}} \quad X_{H_2} (\%) = 100 \cdot \frac{H_2^{in} - H_2^{out}}{H_2^{in}}$$

The selectivity of the different products (S_Z) was calculated as follows:

$$S_Z (\%) = 100 \cdot \frac{n \cdot Z^{out}}{CO_2^{in} - CO_2^{out}} \quad S_{C_{5+}} (\%) = 100 - \sum S_Z$$

n = number of carbon atoms in Z .

The yields were calculated as follows:

$$Y_Z (\%) = \frac{X_{CO_2} \cdot S_Z}{100}$$

$$Y_Z (\text{mol}_{CO_2 \text{ converted to } Z} \text{ mol}_{Me}^{-1} \text{ h}^{-1}) = \frac{(Y_Z (\%)/100) \cdot CO_2^{in} (\text{mol h}^{-1})}{\text{mol}_{Me} (\text{mol})}$$

$Z = CH_4, CO, C_{2+}, C_{5+}$.

STY was calculated as follows:

$$\text{STY} (\text{mol}_{CO_2} \text{ mol}_{Me}^{-1} \text{ h}^{-1}) = \frac{(X_{CO_2} (\%)/100) \cdot CO_2^{in} (\text{mol h}^{-1})}{\text{mol}_{Me} (\text{mol})}$$

3. Results and discussion

Before metal deposition, we modified a commercial TiO_2 support (TiO_2 -P25) through reduction by $NaBH_4$ to introduce

Table 1 Nominal and real metal loading (ICP-OES) of the different catalysts of this study

Catalyst	Nominal (wt%)		ICP-OES (wt%)			
	Co	Pd	Co	Pd	Na	B
1Pd/ TiO_2^*	—	1	—	0.87	0.26	0.01
10Co/ TiO_2^*	10	—	9.70	—	0.64	0.04
0.1Pd-10Co-o/ TiO_2^*	10	0.1	9.98	0.03	0.30	0.02
0.1Pd-10Co-r/ TiO_2^*	10	0.1	10.00	0.09	0.23	0.01
1Pd-10Co-o/ TiO_2^*	10	1	9.65	0.92	0.23	0.02

controlled amounts of promoters (B and particularly Na) as well as oxygen vacancies (O_v) that can be useful for CO_2 activation.¹¹ The underlying effects of Na, B and O_v on the catalytic performance of Co/ TiO_2 catalysts for CO_2 -FTS have been discussed elsewhere.¹¹ The complete characterization of this modified support (TiO_2^*) has already been reported.¹¹ The TiO_2^* , which contains 0.5–0.7% of Na (batch to batch variation), was used to prepare monometallic Co and Pd catalysts as well as bimetallic PdCo catalysts. Table 1 gives the nominal and real metal loading (ICP-OES) of the catalysts. In most cases, ICP-OES results were close to the nominal metal contents, except in the case of the 0.1Pd-10Co-o/ TiO_2^* catalyst (Pd = 0.03 wt%). As far as the Na content is concerned, all samples containing Pd show a lower Na content than TiO_2^* or 10Co/ TiO_2^* . This was attributed to a double displacement (metathesis) reaction, where palladium nitrate and sodium oxide react to form palladium oxide and sodium nitrate. To validate our approach, we first prepared a 1Pd/ TiO_2^* catalyst from Pd nitrate and evaluated its performance for the RWGS. XRD analyses (Fig. S1†) show the presence of metallic Pd already on the calcined catalyst, resulting from the defect (O_v) mediated reduction of the Pd precursor.³⁵ Indeed, Pd particles (*ca.* 2 nm) homogeneously distributed on a defective TiO_2 -P25 containing O_v were produced by a redox reaction, in which Pd ions are reduced by electrons trapped in the O_v .³⁶ Metallic Pd was also detected in the reduced 1Pd/ TiO_2^* catalyst. While the weak intensity of the Pd peak does not allow a reliable measurement of the crystallite size by XRD, HAADF-STEM and EDX analyses show that the majority of the Pd particles have an average particle size of 2.5 nm (Fig. S2†). No trace of encapsulation of Pd by a thin TiO_x overlayer (geometric factor of the SMSI effect³⁷) was observed. Pd single atoms are also visible on the HAADF-STEM micrographs. XPS analyses (Fig. S3†) performed after air exposure of the sample confirm the presence of metallic Pd (78.5%) and PdO (21.5%). If 335.2 eV is taken as the reference for the binding energy (BE) of Pd metal $3d_{5/2}$,³⁸ the BE of Pd in the 1Pd/ TiO_2^* catalyst (335.2 eV) does not suggest any charge transfer (resulting from a SMSI effect³⁷) taking place between the Pd particles and the support. The Ti $2p_{3/2}$ BE was measured at 458.7 eV (Ti^{4+}), to be compared to 458.6 eV for the bare support.

The H_2 -TPR profile of this catalyst (Fig. S4a†) shows three main events: the decomposition of palladium β -hydride PdH_x ,³⁹ the reduction of PdO_x (thin surface layer formed during air exposure),^{40,41} and the reduction of the TiO_2 support at high temperature,^{42,43} while a low temperature reduction of the TiO_2 surface through H-spillover from Pd particles cannot be discarded.⁴⁴ The CO_2 -TPD profiles of the Pd catalyst and the TiO_2^* support are shown in Fig. S4b.† From the deconvolutions (Fig. S5†), it can be concluded that compared to the TiO_2^* support, the 1Pd/ TiO_2^* catalyst binds CO_2 more strongly, since all the peaks are shifted to higher temperatures. Such a phenomenon has already been reported for Pd/ TiO_2 ⁴⁵ and Pt/ TiO_2 catalysts,^{46,47} suggesting an

increased surface basicity upon noble metal addition. The peak at around 100 °C has been attributed to the desorption signal of CO₂ weakly interacting with the TiO₂ support (weak surface basic sites).⁴⁸ At higher temperatures, desorption of adsorbed CO₂ species occurs from carbonate, bicarbonate and formate species (medium surface basic sites). Quantification of the CO₂-TPD results (Table S1†) shows that the catalyst adsorbs less CO₂ than the TiO₂* support, as already reported for Pt/TiO₂ catalysts.⁴⁶ This might be due to a decrease of adsorption sites (O_v and surface Na) after Pd deposition. It is nevertheless important to note that the presence of Pd during catalysis may lead to the generation of O_v and Ti³⁺ sites on the support, which are favorable for strong or medium adsorption of CO₂.^{49,50} The mechanism of CO₂ adsorption on Pd/TiO₂ has been investigated using DFT calculations.⁵¹ It was shown that the interface between Pd and TiO₂ serves as active sites for CO₂ adsorption. CO₂ adsorbed at the interface is activated (bent, CO₂^{δ-}) due to charge transfer from the catalyst, in agreement with the charge density difference and Mulliken charge analysis. Moreover, the binding energy of CO₂ to the interfacial sites is higher than that of CO₂ adsorbed on the pure TiO₂ and Pd surfaces.

As shown in Fig. S6† under RWGSR conditions (H₂/CO₂ = 1, T = 220 °C, P = 20 bar, WHSV = 1620 mL g_{cat}⁻¹ h⁻¹, 60 h on stream), the 1Pd/TiO₂* catalyst produces CO with 100% selectivity. Since this catalyst should operate under FTS conditions, we also investigated its performance for the RWGSR using a H₂/CO₂ of 2. Under these latter conditions (Fig. S6†), the catalyst is still very selective to CO (S_{CO} = 94%). It does not produce methane, but small amounts of C₅₊, probably by a RWGSR + CO hydrogenation route. This is a surprising result since Pd/TiO₂ catalysts have been reported to produce mainly CH₄ and/or CH₃OH under CO hydrogenation conditions.⁵²⁻⁵⁴ Since H species resulting from H-spillover could be involved in CO₂ activation/reduction,⁵⁵ we also investigated the H-spillover on this catalyst. WO₃ was used to diagnose H₂ activation, since it is known that the spilt-over H species produced on noble metal particles can migrate and readily react with WO₃ (yellow powder) to form dark blue H_xWO₃.⁵⁶ It has to be noted that molecular H₂ can reduce the WO₃ only above 200 °C. As expected, and shown in the digital photographs in Fig. S7† taken after treatment with H₂ at 40 °C for 5 min, the WO₃ powder alone does not change color. The dark blue color observed after the test when the WO₃ powder is mixed with the 1Pd/TiO₂* catalyst is indicative of an extended H-spillover on this catalyst. Since H-spillover is often postulated when a dilution of the catalyst leads to an increase of activity in hydrogenation reactions,⁵⁷⁻⁵⁹ we performed an additional experiment where the 1Pd/TiO₂* catalyst was diluted in TiO₂. The significant increase of the CO₂ and H₂ conversions (X_{CO₂}/X_{H₂} = 0.9) and S_{C₅₊} upon dilution (Fig. S6†) can be understood if one admits that CO₂ adsorbed on the support is hydrogenated by the spilt-over hydrogen, which migrates from the surface of the

Pd particles to the surface of the diluent particles. This constitutes an interesting result because it is generally accepted that in CO-FTS, the role of H species resulting from H-spillover is limited to the reduction of cobalt, and their involvement in the direct reduction of CO or CO₂ has only been discussed episodically.^{55,60-64}

Pd being the active phase for the RWGSR, the preparation of a catalyst combining Pd and Co on the same support should guarantee the accessibility of the noble metal to the reactive gases. Consequently, any Pd embedding should be avoided. Co-deposition of Pd and Co (co-impregnation) could result in the formation of an alloy.⁶⁵ Thus, Pd should be deposited by sequential impregnation on the preformed Co/TiO₂* catalyst. Sequential deposition of Co followed by Pd can result in a core-shell structure,⁶⁶ and it was also shown that evaporated Pd metal preferentially nucleates on Co particles previously deposited on a thin alumina film.⁶⁷ Moreover, the CO binding energy to both Pd and Co sites is lowered by the presence of the other metal, favoring subsequent CO-FTS.⁶⁷ For the sequential deposition strategy, in which an exposure of Pd is targeted, different configurations can be envisaged: (A) the two active metals can be separate on the support surface as monometallic particles; (B) the two active metals can be associated in different configurations (alloys, Janus, core@shell);⁶⁸⁻⁷⁰ or (C) a mixture of separated monometallic particles and associated Pd-Co particles. Configuration A and B would be ideal for studying the effects of different Pd locations with respect to Co. However, the exclusive deposition of Pd, non-associated to Co, on a support on which Co particles have already been deposited (configuration A) is highly challenging if not impossible. Moreover, due to the widespread presence of Co (10 wt%, Table 1), both as particles and as clusters,¹¹ the catalyst configuration would likely evolve toward a mixture of monometallic and associated Pd-Co particles under pretreatment or reaction conditions (configuration C). In order to study the effects of Pd location with respect to Co, we have initially prepared bimetallic catalysts presenting a low Pd loading (0.1 wt%). Configurations B and C were obtained by galvanic displacement of Co by Pd,⁷¹ on the reduced catalyst (10Co-r/TiO₂*) and wet sequential impregnation of Pd on the calcined catalyst (10Co-o/TiO₂*), respectively. As the combination of isolated Pd particles and Pd-Co associated particles (configuration C) gave the best results (*vide infra*), this configuration was also attempted with a higher Pd loading (1 wt%). The first catalyst, 0.1Pd-10Co-o/TiO₂*, was prepared through the sequential wet impregnation procedure on 10Co-o/TiO₂*, which resulted in a mixture of separated monometallic particles and associated Pd-Co particles (configuration C). For this bimetallic catalyst, Pd (0.03% wt%, Table 1) can be deposited on both the Co₃O₄ particles and the TiO₂ support. In this catalyst, the Pd loading significantly deviates from the theoretical value. We attribute this difference to a lower

temperature during impregnation. STEM-EDX analysis performed on the reduced $0.1\text{Pd-}10\text{Co-o/TiO}_2^*$ catalyst shows few isolated Pd particles (Fig. S8a†) and some Pd associated to Co (Fig. S8b†). The very low Pd loading (0.03% wt%) and the broad size distribution of Co on Co/TiO_2^* ,¹¹ which is present both as large NPs (>30 nm crystallite) and small clusters (Fig. S9†), render difficult a more detailed analysis of the sample after Pd deposition. To further investigate the effect of Pd location, a second catalyst ($0.1\text{Pd-}10\text{Co-r/TiO}_2$), in which Pd is mostly deposited on reduced Co particles, was prepared from Pd nitrate on the reduced 10Co-r/TiO_2^* catalyst through the galvanic replacement reaction. STEM-EDX analyses confirm that on this sample, Pd (0.09% wt%, Table 1) is associated with Co (Fig. S8c†). To investigate the effect of Pd loading, a third catalyst was prepared by wet impregnation from Pd nitrate on the calcined 10Co/TiO_2^* catalyst with 1 wt% nominal Pd loading ($1\text{Pd-}10\text{Co-o/TiO}_2^*$). STEM-EDX characterization confirms that as for the $0.1\text{Pd-}10\text{Co-o/TiO}_2^*$ catalyst, Pd (0.92% wt%, Table 1) was deposited on both Co_3O_4 and TiO_2 particles (Fig. 1a).

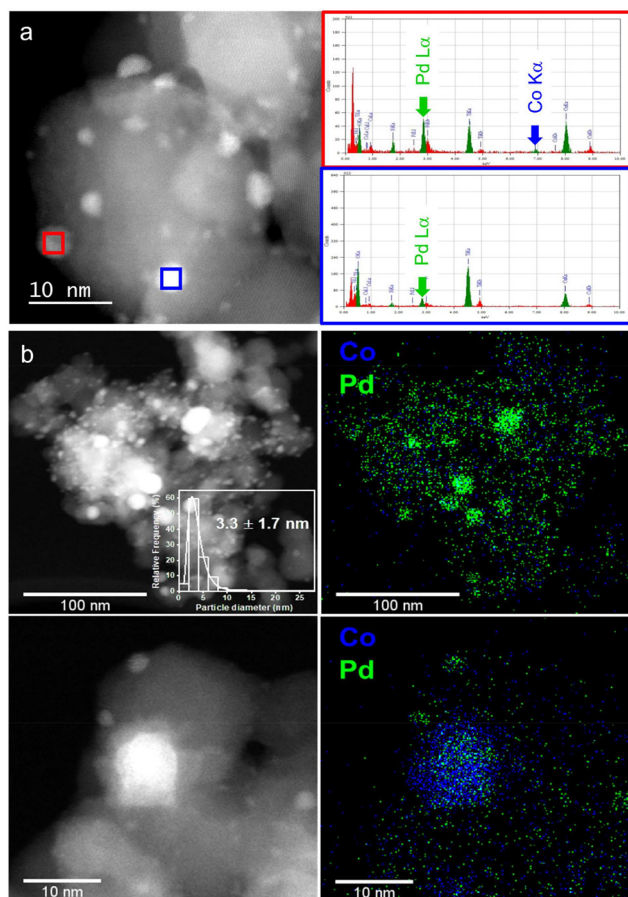


Fig. 1 (a) STEM-HAADF micrograph and EDX analysis showing Pd particles associated with Co (red square) and monometallic Pd particles (blue square) on the sample $1\text{Pd-}10\text{Co-o/TiO}_2^*$ catalyst. (b) HAADF-STEM micrographs with Pd particle size distribution and EDX mapping of the $1\text{Pd-}10\text{Co-o/TiO}_2^*$ catalyst.

In comparison with the catalysts containing 0.1 wt% Pd, the higher Pd loading allows an easier detection of several monometallic Pd particles. The determination of the Pd particle size distribution could be done from more than 200 particles (Fig. 1b). This catalyst mainly contains small Pd particles (3.3 nm) and a few larger ones (20–30 nm). XRD results (Fig. S10†) show the presence of Pd crystallites of an average size of 35 nm (Scherrer equation). For highly or fairly highly dispersed catalysts, the Pd crystallite size, as directly obtained by the XRD line broadening method only, is strongly overestimated.^{72,73} Indeed, the XRD line broadening technique is not able to measure directly very small metal particles ($r \leq 2.5$ nm), because they give diffuse X-ray scattering spreading out into the background. XPS analyses were performed without exposing the sample to the air. The XPS spectra are displayed in Fig. S11.† Pd is exclusively present in its metallic form. The Pd $3d_{5/2}$ BE of this sample (334.7 eV) shifts to a lower value as compared to that of metallic Pd (335.2 eV), consistent with electron-rich Pd species. Similarly, metallic Co presents a shift at lower BE (777.7 eV) compared to the reference value for $\text{Co}^{(0)}$ (778.1 eV).⁷⁴ Nonetheless, most of surface cobalt (83%) is oxidized, with a BE shift to a higher value (780.5 eV) than that of the Co^{2+} reference (780 eV),⁷⁴ indicating the presence of electron-deficient species. The Ti $2p_{3/2}$ BE was measured at 458.8 eV

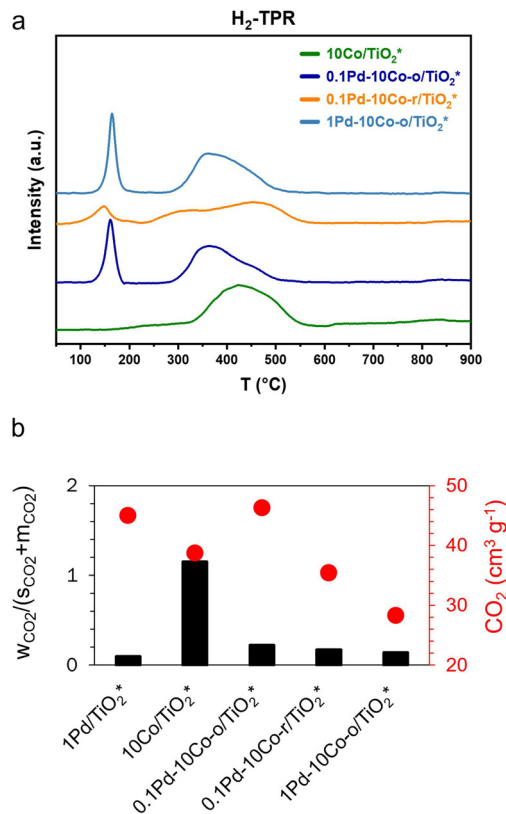


Fig. 2 (a) H₂-TPR profiles of the Co/TiO_2^* and bimetallic catalysts. (b) CO₂-TPD results for the Co/TiO_2^* and bimetallic Pd-Co catalysts. w_{CO_2} = CO₂ weakly adsorbed; s_{CO_2} = CO₂ strongly adsorbed; and m_{CO_2} = CO₂ in the medium adsorption range.

(Ti⁴⁺). Considering that no charge transfer for the 1Pd/TiO₂* catalyst was measured, for which Pd is exclusively on titania, and considering the BE of Pd and Co, a charge transfer occurs from cobalt oxide to Pd due to electronegativity difference and lattice strain.⁷⁵ This result suggests that a significant portion of Pd should be located on cobalt in the 1Pd-10Co-o/TiO₂* catalyst.

H₂-TPR analyses were performed to evaluate the influence of Pd on the reducibility of cobalt (Fig. 2a and Table S2†). Significant differences can be observed in the H₂-TPR profiles of the catalysts. Overall and as expected,⁷⁶ Pd promotion increases cobalt reducibility: all bimetallic catalysts show a significant shift of the Co₃O₄ reduction to CoO at temperatures between 145 and 165 °C, while this step takes place above 300 °C in the case of the unpromoted 10Co/TiO₂* catalyst. This should be correlated to H-spillover from Pd to Co, a well-established phenomenon for Pd/TiO₂ catalysts.^{44,77} However, 0.1Pd-10Co-r/TiO₂* shows broader peaks than the other bimetallic catalysts. For this catalyst, the shift of the first reduction peak at 148 °C (*vs.* 161 °C for the other bimetallic catalysts) and the beginning of the second reduction of CoO to Co at 230 °C (*vs.* 270 °C) suggest an initial increased reducibility of the cobalt oxides. Afterwards, the reduction seems to proceed with difficulty, as shown by the broadness of the peaks and the final reduction being shifted at higher temperature, as in the case of the unpromoted 10Co/TiO₂* catalyst. The initial increased reducibility can be attributed to the fact that in this catalyst cobalt particles are associated with Pd. In that case, the H-spillover process should be, like in single alloy catalysts,⁷⁸ more efficient as it does not involve the support. The subsequent slower reduction might have a different explanation. It might be due to the low Pd loading and/or to a SMSI effect (formation of CoO_x layers on Pd) as reported for the Pd/FeO_x system.⁷⁹

CO₂-TPD experiments were also performed on these catalysts and compared to the ones obtained with the monometallic catalysts. Deconvolution of the spectra is shown in Fig. S12† and the results of quantifications are shown in Table S1.† All catalysts adsorbed CO₂ in the weak (*w*_{CO₂}), medium (*m*_{CO₂}) and strong (*s*_{CO₂}) adsorption range. In general, a too weak or too strong CO₂ adsorption is not favorable for CO₂ hydrogenation. The weakly adsorbed CO₂ cannot be activated, and the strongly adsorbed CO₂ cannot be easily reduced.⁸⁰ Compared to the 10Co/TiO₂* catalyst, which adsorbed CO₂ mainly in the weak adsorption range, all bimetallic catalysts show an adsorption shifted in the strong and particularly in the medium adsorption range (Fig. 2b and S12†). This should positively impact the catalyst activity. For the bimetallic catalyst series, the total amount of adsorbed CO₂ and the ratio *w*_{CO₂}/(*s*_{CO₂} + *m*_{CO₂}) are decreasing when increasing the Pd loading. Overall, the characterization results suggest that the presence of Pd not only influences the overall Co reducibility but also the amount and adsorption strength of CO₂. Regarding the activity of Pd for

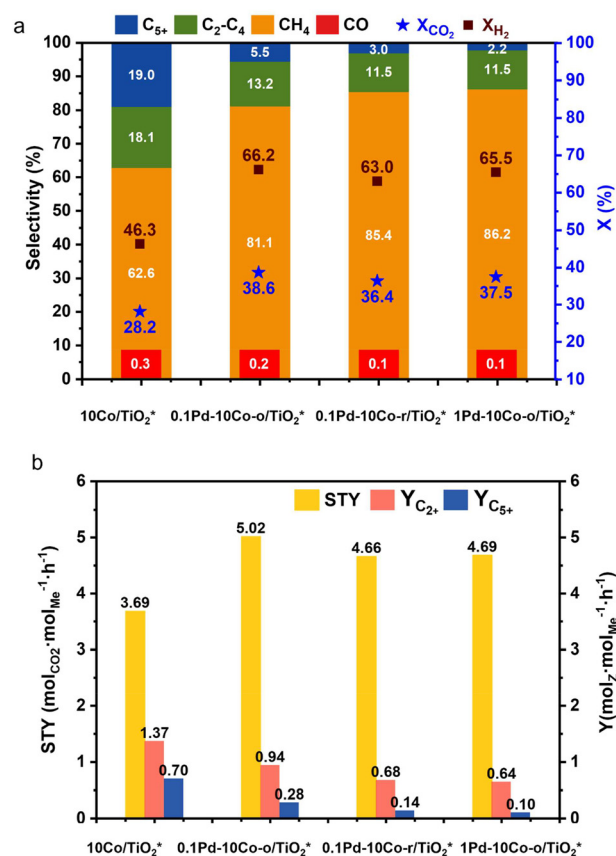


Fig. 3 (a) Conversions (*X*, blue and wine) and selectivity (white), CO selectivity in red. (b) STY (mol_{CO₂} mol_{Me}⁻¹ h⁻¹) and yields (*Y*, mol_Z mol_{Me}⁻¹ h⁻¹, Z = C₂+, C₅+) of the catalysts at 25 hours on stream, T = 220 °C, P = 20 bar, WHSV = 1620 mL g_{cat}⁻¹ h⁻¹.

the RWGSR in bimetallic catalysts, it is interesting to note that PdCo bimetallic catalysts have been reported to be active and selective catalysts for the RWGSR.⁸¹⁻⁸³

The 10Co/TiO₂* and bimetallic catalysts were tested for CO₂-FTS. In a typical experiment, 2 g of calcined catalyst were diluted with 8 g of inert SiC. The catalytic results after 25 h on stream (Fig. 3) show that all the Pd-doped catalysts are more active than 10Co/TiO₂*. It is worth mentioning that these catalysts show appreciable CO₂ conversion at relatively low temperature (220 °C), which is normally not reached on conventional Co/TiO₂ (ref. 80) or Ni/TiO₂ methanation catalysts.⁸⁴ Several parameters such as (i) the Pd loading (measured by ICP), (ii) the CO₂ adsorption capacity in the medium/strong range (measured by TPD), and (iii) the ability to activate H₂ (measured by TPR) that facilitate Co reduction *via* H-spillover, can be at the origin of the observed activity enhancement on the Pd-doped catalysts. The effect of H-spillover from noble metal promoters is not limited to Co reduction, but has also been proposed to influence the cobalt activity and CH₄ selectivity during the CO-FTS reaction.^{33,63,64} These parameters do not all impact in the same way the three bimetallic catalysts studied. For example, catalyst 0.1Pd-10Co-o/TiO₂* has the lowest Pd loading, shows an

intermediate Co reduction but allows optimal CO₂ adsorption.

Fig. S13a† shows a radar chart including the main measured parameters (Pd loading, CO₂ adsorption capacity in the medium/strong range and ability to activate H₂) and the measured STY, all on a 0–1 scale. It is clear from this diagram that in the investigated range, the Pd loading should not have a pronounced effect on the catalyst activity. Although differences in STY between the bimetallic catalysts are not pronounced, we tried to correlate the different parameters, both independently and in combination, with the STY values. A perfect correlation was found between STY and a combination of the CO₂ adsorption capacity in the medium/strong range and the ability to activate H₂ (Fig. S13b†). A similar tendency (*i.e.* higher STY with higher CO₂ adsorption capacity in the medium/strong range and ability to activate H₂) was observed when including the 10Co/TiO₂* catalyst (Fig. S13c†).

Fig. 3 also shows that the higher STY obtained on the bimetallic catalysts is related to an increased CH₄ formation, with a consequent reduction of the selectivity and yields of C₂₊ and particularly C₅₊ products. A detailed characterization of the C₅₊ distribution would require very long tests (>300 h), which was practically impossible for the present study. The lower methane selectivity obtained on the 10Co/TiO₂* catalyst could in part be related to its higher Na content (Table 1). Indeed, besides improving CO₂ activation and limiting H₂ activation, the presence of sodium on the support allows a modulation of H-spillover in the system, which in turn allows an optimal surface C/H ratio on cobalt to produce higher hydrocarbons.¹¹ Increased CO₂ conversion and CH₄ selectivity with a detrimental effect on C₅₊ hydrocarbons has been reported for low pressure (1 bar) CO₂ hydrogenation on Pd-promoted Co/SiO₂ catalysts.¹⁵ In conventional CO-FTS on Pd-Co catalysts, contrasting results have been reported concerning the evolution of activity and selectivity upon Pd doping. For Pd-Co/Al₂O₃ catalysts prepared by sequential impregnation, it was reported that the Pd doping contributes to an increase⁸⁵ or not⁸⁶ of the CH₄ selectivity. An increase of CO conversion and CH₄ selectivity was reported on Pd-Co/SiO₂ catalysts, in which Pd formed well-dispersed alloyed particles with Co.⁸⁷ On the SBA-15 silica, it was shown that the procedure of catalyst preparation affects their performances. Pd-Co/SBA-15 catalysts prepared by co-impregnation were less active and more selective to CH₄ than the ones prepared by sequential impregnation (first Co then Pd).⁸⁸ The higher CH₄ selectivity measured for the catalyst prepared by co-impregnation was attributed to a better mixing of Co and Pd, which resulted in a faster hydrogenation rate. A similar tendency was observed for our two low Pd loading catalysts. When Pd is mainly located on cobalt as in the 0.1Pd-10Co-r/TiO₂* sample, the catalyst is a little less active and more selective towards CH₄ compared to the 0.1Pd-10Co-o/TiO₂* catalyst, for which Pd is located on both the support and cobalt. Overall, it appears that among

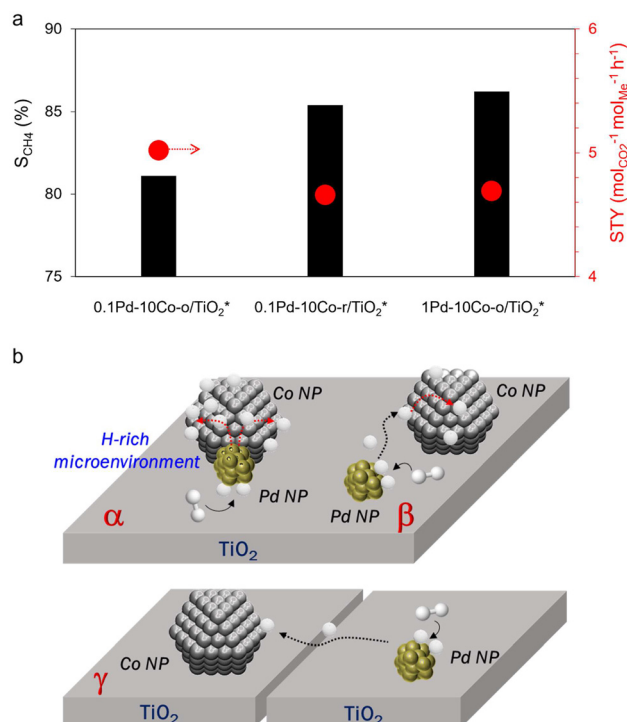


Fig. 4 (a) Performances of the Pd-doped catalysts. (b) Illustration of H-spillover-assisted CH₄ formation on bimetallic (Co-Pd) and monometallic (Co + Pd) catalysts. Configuration α (Co-Pd), where Pd and Co are in direct contact, facilitates the process. In configuration β (Co-Pd), the H spilt-over species have to diffuse on the support, slowing down the process. In configuration γ (Co + Pd), there is a physical separation of Pd from Co on two different supports.

the catalysts doped with Pd, the most active one (0.1Pd-10Co-o/TiO₂*) is also the least selective for methane (Fig. 4a). Considering the difference in catalyst preparation and in metal loading, this catalyst should be the one presenting the lower amount of Pd on cobalt.

For the two other catalysts, because of different preparation procedures and/or metal loading, the concentration of Pd in direct contact with cobalt should be significantly higher. This latter situation (Fig. 4b, configuration α) should increase the H*/CO* ratio on cobalt due to the facile H-spillover from Pd to Co leading to higher CH₄ selectivity.⁹ As far as the RWGSR activity of Pd particles in configuration α is concerned, it should not decrease because they are in contact with cobalt.^{82,83} In configuration β of Fig. 4b, the fact that H species should diffuse on the support before reaching the Co particles should lower the H*/CO* ratio. As H-spillover seems to play an important role in the catalytic performances, we evaluated its extent experimentally (Fig. S7†). When WO₃ is mixed with the Co/TiO₂* catalyst, no H-spillover occurs at 40 °C. This is not surprising since a moderate H-spillover was noticed for this catalyst only at 180 °C.¹¹ For all the Pd-modified Co/TiO₂* catalysts, H-spillover operates at 40 °C. If we consider the color changes, from dark blue for 1Pd/TiO₂* to pale blue for

0.1Pd-10Co-r/TiO₂* (Fig. S7†), the following order can be proposed for the extent of H-spillover on the TiO₂ surface: 1Pd/TiO₂* > 1Pd-10Co-o/TiO₂* > 0.1Pd-10Co-o/TiO₂* > 0.1Pd-10Co-r/TiO₂*. It has to be noted that the extent of H-spillover is higher for 0.1Pd-10Co-o/TiO₂* than for 0.1Pd-10Co-r/TiO₂*, despite the fact that the former catalyst contains three times less Pd. Globally, a higher spillover is noticed on the catalysts for which Pd is deposited on the TiO₂ support. Therefore, the catalytic performance reported in Fig. 4a should not be directly related to the extent of the H-spillover but rather to the degree of intimacy between Pd and Co. Finally, to probe further the effect of Pd and Co intimacy on the catalytic performance, we also evaluated the configuration γ of Fig. 4b, involving monometallic catalysts for which there is a physical separation of Pd from Co, that is, by combining a Pd-TiO₂* and a Co-TiO₂* catalyst. In that case, a lower H*/CO* ratio on cobalt can be expected.

As the main limitation of Pd promotion in bimetallic Pd-Co catalysts is the excessive H₂ activation, it might be useful to keep the two metals far away on two different supports. The combination of the two monometallic catalysts (1Pd/TiO₂* and 10Co/TiO₂*) allowed two different configurations of the catalyst bed. In the first one (Fig. S14a,† 2-bed configuration), the two individual catalysts (1 g of 1Pd/TiO₂* and 1 g of 10Co/TiO₂*, each diluted with 4 g of SiC powder) are placed in two distinct layers separated by a thin layer of quartz wool. The inlet gas first passes through the 1Pd/TiO₂* catalyst before reaching the 10Co/TiO₂* catalyst. According to the support used (non-reducible *vs.* reducible) and operating conditions, migration/diffusion distances of a few nanometers to several millimeters have been reported for spillover of hydrogen species.^{17,89-91} The presence of water⁹² or oxygenated organic molecules⁹³ in the gas phase facilitates the phenomenon. Some studies have also proposed that the phenomenon can also occur when two beds of monometallic catalysts are separated by a material allowing secondary spillover.^{17,60} In the second configuration (Fig. S14b,† 1-bed configuration), the two powders (1 g of each) are physically mixed and diluted with 8 g of SiC. Such a configuration was used to compare the reactivity of a physical mixture of catalysts (Pt/Al₂O₃ + Co/Al₂O₃) to bimetallic Pt-Co/Al₂O₃ catalysts for CO-FTS.⁶³ Despite an improved reducibility of Co for both systems, the effect of Pt on catalyst performance was significantly diminished when using a physical mixture. It was suggested that the larger distance between Pt and Co severely diminished the flux of spilt-over hydrogen species on this non-reducible oxide.

The catalytic results are shown in Fig. 5. For these two specific configurations, the metal content (Co and Pd) was reduced by half while keeping the same metal loading for each catalyst. Both configurations outperform the 10Co/TiO₂* and the bimetallic catalysts in terms of STY, Y_{C₂₊} and Y_{C₅₊} (Fig. 5b). Due to the low metal loading in the 1Pd/TiO₂* catalyst, a larger amount of TiO₂* surface is exposed for both

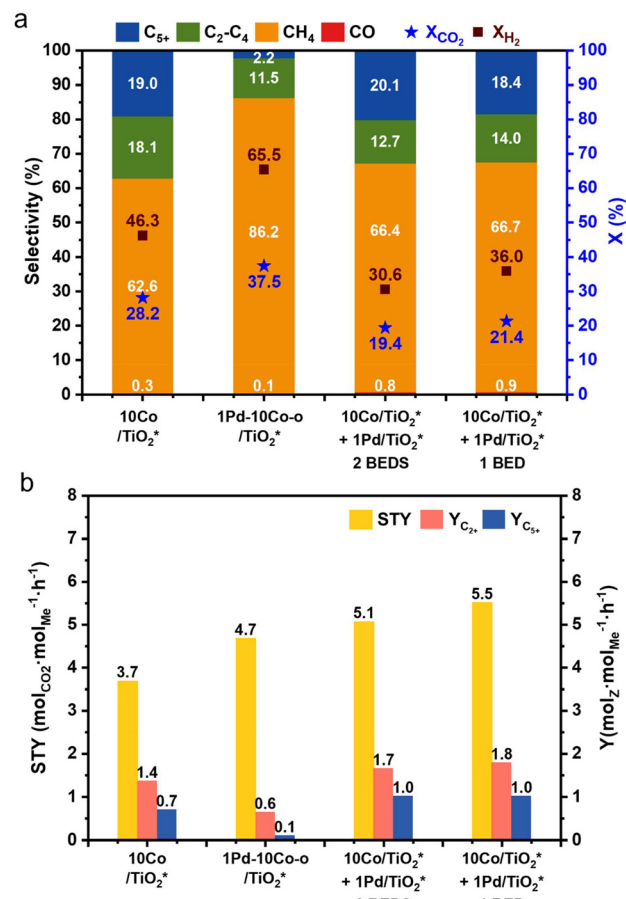


Fig. 5 (a) Conversions (X , blue and wine) and selectivity (white). (b) STY (mol_{CO₂} mol_{Me}⁻¹ h⁻¹) and yields (Y , mol_Z mol_{Me}⁻¹ h⁻¹, $Z = C_{2+}$, C_{5+}) of the catalysts at 25 h on stream, $T = 220$ °C, $P = 20$ bar, WHSV = 1620 mL g_{cat}⁻¹ h⁻¹.

monometallic configurations as compared to Co/TiO₂* or to the bimetallic systems. The higher TiO₂* surface area should play an active role in CO₂ adsorption and activation.¹¹ An enhanced CO₂ adsorption combined with a limited concentration of H species resulting from H-spillover should result in optimized catalytic performances for both monometallic configurations. It is also worth reminding that the combination of the two monometallic catalysts implied the use of the 10Co/TiO₂* catalyst, which contains more Na. This can also contribute to limiting the H-spillover. Between the two configurations, the best conversions are obtained with the 1-bed configuration.

The intimate contact between the two powders in this configuration should result in an enhanced H-spillover, which should be at the origin of an enhanced activity. Small differences in the selectivity are observed for the tests performed in the 1-bed and 2-bed configurations. Indeed, in comparison with the 2-bed configuration, the 1-bed configuration allows a slightly higher selectivity towards C₂-C₄ and lower selectivity towards C₅₊. Such differences are ascribable to a higher H₂ activation during the test in the

1-bed configuration, leading to a higher X_{H_2}/X_{CO_2} ratio than in the 2-bed configuration. The higher H-coverage of Co particles should favor C_2 – C_4 products over C_{5+} ones. Finally, if we consider the STY and C_{2+} yield, the most efficient system investigated in this study consists in a mixture of monometallic catalysts in a single-bed configuration (Fig. S15†). This system should constitute the best compromise between Co and Pd intimacy, free TiO_2^* surface and extent of H-spillover. These results confirm that the configuration γ of Fig. 4b (mixture of monometallic catalysts), for which there is a physical separation of Pd from Co on two different supports, should favor a lower H^*/CO^* ratio on cobalt than in the case of bimetallic catalysts, resulting in higher selectivity towards C_{5+} .

4. Conclusions

This study describes the use of Pd as a co-catalyst to increase the performance of an alkali-promoted Co/ TiO_2 catalyst during CO_2 -FTS. Palladium was chosen since it is active for the RWGS, and it is employed to promote Co-based CO -FTS catalysts by improving the cobalt reducibility thanks to H-spillover.

Under CO_2 -FTS conditions, Pd/ TiO_2^* is active for the RWGS and also produces small amounts of C_{5+} . Two systems were investigated: bimetallic catalysts and mixtures of monometallic catalysts. Hydrogen spillover contributes to an easier Co reduction in all these systems. For all systems investigated, the addition of Pd to the Co/ TiO_2^* catalyst allows a significant increase of the STY.

For bimetallic catalysts, the effects of both Pd location with respect to Co and the metal loading on the catalytic performances were investigated. All bimetallic catalysts are more active but less selective in C_{5+} than the Co/ TiO_2^* catalyst. The STY of the bimetallic catalysts correlates well with CO_2 adsorption capacity in the medium/strong range and ability to activate H_2 . The catalytic performances (STY and S_{CH_4}) were not directly related to the extent of the H-spillover but rather to the degree of intimacy between Pd and Co. A high intimacy favors a H-rich microenvironment around the cobalt that should affect the H^*/CO^* ratio on cobalt and as a consequence decreases the selectivity towards C_{5+} . Increasing Pd metal loading does not lead to performance improvement.

The separation of the two metals on two different supports strongly benefits not only STY but also C_{2+} and C_{5+} yields since it should decrease the H^*/CO^* ratio on cobalt. The single-bed configuration (one bed with a mixture of monometallic catalysts) constitutes the best compromise between Co and Pd intimacy, free TiO_2^* surface and extent of H-spillover. Consequently, the promotion of Co/ TiO_2 catalysts by palladium for the CO_2 -FTS is better achieved with mixtures of monometallic catalysts than with bimetallic catalysts.

These results emphasize the importance of the intimacy criterion in bimetallic/bifunctional catalytic systems involving

H-spillover phenomena. Consideration of the spatial distribution of both metals should allow significant advances in the field of catalytic reactions involving hydrogen and, in a broader context, for the hydrogen-based economy.

Author contributions

C. S.: methodology, investigation and writing – original draft preparation. A. D.: investigation. Y. T.: XPS measurements, analysis. D. P. M.: conceptualisation, visualisation, validation, writing – review & editing and resources. K. S.: conceptualisation, visualisation, validation, writing – review & editing and resources. P. S.: conceptualisation, visualisation, validation, writing – review & editing and resources.

Conflicts of interest

There are no conflicts to declare.

Acknowledgements

This work was supported by the Agence Nationale de la Recherche (project ANR-19-CE07-0030) and partially financed by ALTENS. This study was labeled by the EUR BIOECO under the “Investissements d’Avenir” program with reference ANR-18-EURE-0021, which is gratefully acknowledged. The authors thank Teresa Hungria (Centre de microcaractérisation Raimond Castaing) for the STEM-HAADF/EDX microscopy, and the technicians at the RAPSODEE center for technical assistance during the CO_2 -FTS tests.

Notes and references

- 1 Y. Wang, Y. Tian, S.-Y. Pan and S. W. Snyder, *ChemSusChem*, 2022, **15**, e202201290.
- 2 C. Vogt, M. Monai, G. J. Kramer and B. M. Weckhuysen, *Nat. Catal.*, 2019, **2**, 188–197.
- 3 C. Scarfiello, D. Pham Minh, K. Soulantica and P. Serp, *Adv. Mater. Interfaces*, 2023, **10**, 2202516.
- 4 C. Panzone, R. Philippe, A. Chappaz, P. Fongarland and A. Bengaouer, *J. CO2 Util.*, 2020, **38**, 314–347.
- 5 B. Yao, T. Xiao, O. A. Makgae, X. Jie, S. Gonzalez-Cortes, S. Guan, A. I. Kirkland, J. R. Dilworth, H. A. Al-Megren, S. M. Alshihri, P. J. Dobson, G. P. Owen, J. M. Thomas and P. P. Edwards, *Nat. Commun.*, 2020, **11**, 6395.
- 6 G. Prieto, *ChemSusChem*, 2017, **10**, 1056–1070.
- 7 W. Ma, G. Jacobs, D. E. Sparks, B. Todic, D. B. Bukur and B. H. Davis, *Catal. Today*, 2020, **343**, 125–136.
- 8 R.-P. Ye, J. Ding, W. Gong, M. D. Argyle, Q. Zhong, Y. Wang, C. K. Russell, Z. Xu, A. G. Russell, Q. Li, M. Fan and Y.-G. Yao, *Nat. Commun.*, 2019, **10**, 5698.
- 9 P. Bredy, D. Farrusseng, Y. Schuurman and F. C. Meunier, *J. Catal.*, 2022, **411**, 93–96.
- 10 W. W. Russell and G. H. Miller, *J. Am. Chem. Soc.*, 1950, **72**, 2446–2454.
- 11 C. Scarfiello, K. Soulantica, S. Cayez, A. Durupt, G. Viau, N. Le Breton, A. K. Boudalis, F. Meunier, G. Clet, M. Barreau, D.

- Salusso, S. Zafeiratos, D. P. Minh and P. Serp, *J. Catal.*, 2023, **428**, 115202.
- 12 I. C. ten Have and B. M. Weckhuysen, *Chem Catal.*, 2021, **1**, 339–363.
- 13 M. D. Porosoff and J. G. Chen, *J. Catal.*, 2013, **301**, 30–37.
- 14 R. E. Owen, J. P. O’Byrne, D. Mattia, P. Plucinski, S. I. Pascu and M. D. Jones, *Chem. Commun.*, 2013, **49**, 11683–11685.
- 15 R. A. Iloy, K. Jalama and P. R. Khangale, *Catal. Lett.*, 2024, DOI: [10.1007/s10562-023-04527-4](https://doi.org/10.1007/s10562-023-04527-4).
- 16 F. Diehl and A. Y. Khodakov, *Oil Gas Sci. Technol.*, 2009, **64**, 11–24.
- 17 P. Baeza, M. S. Ureta-Zañartu, N. Escalona, J. Ojeda, F. J. Gil-Llambias and B. Delmon, *Appl. Catal., A*, 2004, **274**, 303–309.
- 18 L. Xiong, S. Liu, Y. Men, L. Li, X. Niu, K. Guo, J. Xu, W. An, J. Wang and Y. Cong, *J. Environ. Chem. Eng.*, 2022, **10**, 108407.
- 19 L.-X. Wang, L. Wang and F.-S. Xiao, *Chem. Sci.*, 2021, **12**, 14660–14673.
- 20 A. M. Bahmanpour, M. Signorile and O. Kröcher, *Appl. Catal., B*, 2021, **295**, 120319.
- 21 J. F. M. Simons, T. J. de Heer, R. C. J. van de Poll, V. Muravev, N. Kosinov and E. J. M. Hensen, *J. Am. Chem. Soc.*, 2023, **145**, 20289–20301.
- 22 A. Parastaev, V. Muravev, E. H. Osta, T. F. Kimpel, J. F. M. Simons, A. J. F. van Hoof, E. Uslamin, L. Zhang, J. J. C. Struijs, D. B. Burueva, E. V. Pokochueva, K. V. Kovtunov, I. V. Koptyug, I. J. Villar-Garcia, C. Escudero, T. Altantzis, P. Liu, A. Béché, S. Bals, N. Kosinov and E. J. M. Hensen, *Nat. Catal.*, 2022, **5**, 1051–1060.
- 23 M. Danielis, J. D. Jiménez, N. Rui, J. Moncada, L. E. Betancourt, A. Trovarelli, J. A. Rodriguez, S. D. Senanayake and S. Colussi, *Appl. Catal., A*, 2023, **660**, 119185.
- 24 X. Wang, H. Shi, J. H. Kwak and J. Szanyi, *ACS Catal.*, 2015, **5**, 6337–6349.
- 25 L. Chen, S. I. Allec, M.-T. Nguyen, L. Kovarik, A. S. Hoffman, J. Hong, D. Meira, H. Shi, S. R. Bare, V.-A. Glezakou, R. Rousseau and J. Szanyi, *J. Am. Chem. Soc.*, 2023, **145**, 10847–10860.
- 26 X. Chen, X. Su, H. Duan, B. Liang, Y. Huang and T. Zhang, *Catal. Today*, 2017, **281**, 312–318.
- 27 L. Chen, R. R. Unocic, A. S. Hoffman, J. Hong, A. H. Braga, Z. Bao, S. R. Bare and J. Szanyi, *JACS Au*, 2021, **1**, 977–986.
- 28 F. Doherty and B. R. Goldsmith, *ChemCatChem*, 2021, **13**, 3155–3164.
- 29 B. Han, Q. Li, X. Jiang, Y. Guo, Q. Jiang, Y. Su, L. Li and B. Qiao, *Small*, 2022, **18**, 2204490.
- 30 Y. Tang, C. Asokan, M. Xu, G. W. Graham, X. Pan, P. Christopher, J. Li and P. Sautet, *Nat. Commun.*, 2019, **10**, 4488.
- 31 S. Kattel, W. Yu, X. Yang, B. Yan, Y. Huang, W. Wan, P. Liu and J. G. Chen, *Angew. Chem., Int. Ed.*, 2016, **55**, 7968–7973.
- 32 H. Wang, M. S. Bootharaju, J. H. Kim, Y. Wang, K. Wang, M. Zhao, R. Zhang, J. Xu, T. Hyeon, X. Wang, S. Song and H. Zhang, *J. Am. Chem. Soc.*, 2023, **145**, 2264–2270.
- 33 T. N. Phaahlamohlaka, D. O. Kumi, M. W. Dlamini, R. Forbes, L. L. Jewell, D. G. Billing and N. J. Coville, *ACS Catal.*, 2017, **7**, 1568–1578.
- 34 M. Tang, P. E. de Jongh and K. P. de Jong, *Small*, 2024, **20**, 2304683.
- 35 X. Pan and Y.-J. Xu, *J. Phys. Chem. C*, 2013, **117**, 17996–18005.
- 36 X. Pan and Y.-J. Xu, *ACS Appl. Mater. Interfaces*, 2014, **6**, 1879–1886.
- 37 W. T. Figueiredo, R. Prakash, C. G. Vieira, D. S. Lima, V. E. Carvalho, E. A. Soares, S. Buchner, H. Raschke, O. W. Perez-Lopez, D. L. Baptista, R. Hergenröder, M. Segala and F. Bernardi, *Appl. Surf. Sci.*, 2022, **574**, 151647.
- 38 M. A. Ehsan, M. Sohail, R. Jamil and A. S. Hakeem, *Electrocatalysis*, 2019, **10**, 214–221.
- 39 C. M. Mendez, H. Olivero, D. E. Damiani and M. A. Volpe, *Appl. Catal., B*, 2008, **84**, 156–161.
- 40 B. Rusinque, S. Escobedo and H. de Lasa, *Catalysts*, 2020, **10**, 74.
- 41 M. He, Y. Cao, J. Ji, K. Li and H. Huang, *J. Catal.*, 2021, **396**, 122–135.
- 42 H. Zhu, Z. Qin, W. Shan, W. Shen and J. Wang, *J. Catal.*, 2004, **225**, 267–277.
- 43 M. G. Rinaudo, A. M. Beltrán, A. Fernández, L. E. Cadús and M. R. Morales, *Results Eng.*, 2022, **16**, 100737.
- 44 M. Yarar, A. Bouziani and D. Uner, *Catal. Commun.*, 2023, **174**, 106580.
- 45 R. Khatun, P. Bhanja, P. Mondal, A. Bhaumik, D. Das and S. Manirul Islam, *New J. Chem.*, 2017, **41**, 12937–12946.
- 46 D. Permporn, R. Khunphonoi, J. Wilamat, P. Khemthong, P. Chirawatkul, T. Butburee, W. Sangkhun, K. Wantala, N. Grisdanurak, J. Santatiwongchai, P. Hirunsit, W. Klysubun and M. D. G. de Luna, *Nanomaterials*, 2022, **12**, 474.
- 47 L.-Y. Lin, S. Kavadiya, X. He, W.-N. Wang, B. B. Karakocak, Y.-C. Lin, M. Y. Berezin and P. Biswas, *Chem. Eng. J.*, 2020, **389**, 123450.
- 48 J. Zhang, W. Liao, H. Zheng, Y. Zhang, L. Xia, B.-T. Teng, J.-Q. Lu, W. Huang and Z. Zhang, *J. Catal.*, 2022, **405**, 152–163.
- 49 M. Shopska, A. Caballero, F. Platero, S. Todorova, K. Tenchev, M. Fabian, K. Aleksieva, H. Kolev and G. Kadinov, *React. Kinet., Mech. Catal.*, 2022, **135**, 589–618.
- 50 J. Panpranot, K. Kontapakdee and P. Prasertthadam, *J. Phys. Chem. B*, 2006, **110**, 8019–8024.
- 51 Z. Ou, J. Ran, J. Niu, C. Qin, W. He and L. Yang, *Int. J. Hydrogen Energy*, 2020, **45**, 6328–6340.
- 52 S. Y. Wang, S. H. Moon and M. A. Vannice, *J. Catal.*, 1981, **71**, 167–174.
- 53 J. D. Bracey and R. Burch, *J. Catal.*, 1984, **86**, 384–391.
- 54 W.-J. Shen, M. Okumura, Y. Matsumura and M. Haruta, *Appl. Catal., A*, 2001, **213**, 225–232.
- 55 F. Solymosi, A. Erdöhelyi and M. Lancz, *J. Catal.*, 1985, **95**, 567–577.
- 56 Y. Xi, Q. Zhang and H. Cheng, *J. Phys. Chem. C*, 2014, **118**, 494–501.
- 57 F. Benseradj, F. Sadi and M. Chater, *Appl. Catal., A*, 2002, **228**, 135–144.
- 58 S. T. Srinivas and P. K. Rao, *J. Catal.*, 1994, **148**, 470–477.

- 59 H. Chen, H. Yang, O. Omotoso, L. Ding, Y. Briker, Y. Zheng and Z. Ring, *Appl. Catal., A*, 2009, **358**, 103–109.
- 60 D. Messou, V. Bernardin, F. Meunier, M. B. Ordoño, A. Urakawa, B. F. Machado, V. Collière, R. Philippe, P. Serp and C. Le Berre, *J. Catal.*, 2021, **398**, 14–28.
- 61 K.-D. Jung and A. T. Bell, *J. Catal.*, 2000, **193**, 207–223.
- 62 D. Xu, X. Hong and G. Liu, *J. Catal.*, 2021, **393**, 207–214.
- 63 D. Nabaho, J. W. Niemantsverdriet, M. Claeys and E. van Steen, *Catal. Today*, 2016, **261**, 17–27.
- 64 A. C. Ghogia, S. Cayez, B. F. Machado, A. Nzihou, P. Serp, K. Soulantica and D. Pham Minh, *ChemCatChem*, 2020, **12**, 1117–1128.
- 65 N. Tsubaki, S. Sun and K. Fujimoto, *J. Catal.*, 2001, **199**, 236–246.
- 66 A. F. Carlsson, M. Naschitzki, M. Bäumer and H. J. Freund, *J. Phys. Chem. B*, 2003, **107**, 778–785.
- 67 A. F. Carlsson, M. Bäumer, T. Risse and H.-J. Freund, *J. Chem. Phys.*, 2003, **119**, 10885–10894.
- 68 M. Sankar, N. Dimitratos, P. J. Miedziak, P. P. Wells, C. J. Kiely and G. J. Hutchings, *Chem. Soc. Rev.*, 2012, **41**, 8099–8139.
- 69 N. Eom, M. E. Messing, J. Johansson and K. Deppert, *ACS Nano*, 2021, **15**, 8883–8895.
- 70 L. Liu and A. Corma, *Chem. Rev.*, 2023, **123**, 4855–4933.
- 71 T. Yoshii, K. Nakatsuka, Y. Kuwahara, K. Mori and Y. Hiromi, *RSC Adv.*, 2017, **7**, 22294–22300.
- 72 G. Fagherazzi, P. Canton, P. Riello, N. Pernicone, F. Pinna and M. Battaglin, *Langmuir*, 2000, **16**, 4539–4546.
- 73 C. Amorim and M. A. Keane, *J. Colloid Interface Sci.*, 2008, **322**, 196–208.
- 74 M. C. Biesinger, B. P. Payne, A. P. Grosvenor, L. W. M. Lau, A. R. Gerson and R. S. C. Smart, *Appl. Surf. Sci.*, 2011, **257**, 2717–2730.
- 75 T. Yang, D. Bhalothia, H.-W. Chang, C. Yan, A. Beniwal, Y.-X. Chang, S.-C. Wu, P.-C. Chen, K.-W. Wang, S. Dai and T.-Y. Chen, *Chem. Eng. J.*, 2023, **454**, 140289.
- 76 P. K. Gupta, A. Mahato, G. K. Gupta, G. Sahu and S. Maity, *Oil Gas Sci. Technol.*, 2021, **76**, 21.
- 77 Z. Tang, Y. Li, K. Zhang, X. Wang, S. Wang, Y. Sun, H. Zhang, S. Li, J. Wang, X. Gao, Z. Hou, L. Shi, Z. Yuan, K. Nie, J. Xie, Z. Yang and Y.-M. Yan, *ACS Energy Lett.*, 2023, **8**, 3945–3954.
- 78 W. Osada, S. Tanaka, K. Mukai, M. Kawamura, Y. Choi, F. Ozaki, T. Ozaki and J. Yoshinobu, *Phys. Chem. Chem. Phys.*, 2022, **24**, 21705–21713.
- 79 J. Liu, L. Wang, F. Okejiri, J. Luo, J. Zhao, P. Zhang, M. Liu, S. Yang, Z. Zhang, W. Song, W. Zhu, J. Liu, Z. Zhao, G. Feng, C. Xu and S. Dai, *ACS Catal.*, 2020, **10**, 8950–8959.
- 80 Z. Qin, X. Wang, L. Dong, T. Su, B. Li, Y. Zhou, Y. Jiang, X. Luo and H. Ji, *Chem. Eng. Sci.*, 2019, **210**, 115245.
- 81 N. Osakoo, P. Tawachkultanadilok, S. Loiha, F. Roessner, Y. Poo-arporn, P. Kidkhunthod, N. Chanlek, S. Prayoonpokarach and J. Wittayakun, *Appl. Catal., B*, 2022, **316**, 121670.
- 82 C. Yan, D. Bhalothia, S.-S. Yang, A. Beniwal, Y.-X. Chang, P.-C. Wang, Y.-C. Cheng, C.-L. Chen, S.-C. Wu and T.-Y. Chen, *Catalysts*, 2022, **12**, 1127.
- 83 D. Bhalothia, S.-S. Yang, C. Yan, A. Beniwal, Y.-X. Chang, S.-C. Wu, P.-C. Chen, K.-W. Wang and T.-Y. Chen, *Sustainable Energy Fuels*, 2023, **7**, 526–536.
- 84 W. L. Vrijburg, E. Moioli, W. Chen, M. Zhang, B. J. P. Terlingen, B. Zijlstra, I. A. W. Filot, A. Züttel, E. A. Pidko and E. J. M. Hensen, *ACS Catal.*, 2019, **9**, 7823–7839.
- 85 W. Ma, G. Jacobs, R. A. Keogh, D. B. Bukur and B. H. Davis, *Appl. Catal., A*, 2012, **437–438**, 1–9.
- 86 D. Xu, W. Li, H. Duan, Q. Ge and H. Xu, *Catal. Lett.*, 2005, **102**, 229–235.
- 87 S. Sun, K. Fujimoto, Y. Yoneyama and N. Tsubaki, *Fuel*, 2002, **81**, 1583–1591.
- 88 N. Osakoo, R. Henkel, S. Loiha, F. Roessner and J. Wittayakun, *Catal. Commun.*, 2015, **66**, 73–78.
- 89 M. Xiong, Z. Gao and Y. Qin, *ACS Catal.*, 2021, **11**, 3159–3172.
- 90 T. Kamada, T. Ueda, S. Fukuura, T. Yumura, S. Hosokawa, T. Tanaka, D. Kan and Y. Shimakawa, *J. Am. Chem. Soc.*, 2023, **145**, 1631–1637.
- 91 J. Lee, P. Tieu, J. Finzel, W. Zang, X. Yan, G. Graham, X. Pan and P. Christopher, *JACS Au*, 2023, **3**, 2299–2313.
- 92 Z. Gu, M. Li, C. Chen, X. Zhang, C. Luo, Y. Yin, R. Su, S. Zhang, Y. Shen, Y. Fu, W. Zhang and F. Huo, *Nat. Commun.*, 2023, **14**, 5836.
- 93 M. Tan, Y. Yang, Y. Yang, J. Chen, Z. Zhang, G. Fu, J. Lin, S. Wan, S. Wang and Y. Wang, *Nat. Commun.*, 2022, **13**, 1457.